Rapid oxidation of phenolic compounds by O_3 and HO•: effects of air-water interface and mineral dust in tropospheric chemical processes

Yanru Huo[a, b], Mingxue Li[c], Xueyu Wang[d], Jianfei Sun[e], Yuxin Zhou[a],

Yuhui Ma[a], Maoxia He[a],*

[a] Environment Research Institute, Shandong University, Qingdao 266237, P. R. China

[b] Department of Atmospheric and Oceanic Sciences, McGill University, 805 Sherbrooke Street West, Montreal, QC, H3A 0B9, Canada

[c] Department of Civil and Environmental Engineering, The Hong Kong Polytechnic University, Hong Kong SAR, China

[d] College of Geography and Environmental Sciences, Zhejiang Normal University, Jinhua 321004, China

[e] School of Environmental and Materials Engineering, Yantai University, Yantai, 264005, PR China

____

*Corresponding author: Prof. Maoxia He

Tel: 86-532-58631972 (o)

Fax: 86-532-5863 1986

E-mail address: hemaox@sdu.edu.cn

Abstract

Environmental media affect the atmospheric oxidation processes of phenolic compounds (PhCs) released from biomass burning in the troposphere. To address the gaps in experimental research, phenol (Ph), 4-hydroxybenzaldehyde (4-HBA), and vanillin (VL) are chosen as model compounds to investigate their reaction mechanism and kinetics at the air-water (A-W) interface, on TiO_2 mineral aerosols, in the gas phase, and in bulk water using a combination of molecular dynamics simulation and quantum chemical calculations. Of them, Ph was the most reactive one. The occurrence percentages of Ph, 4-HBA, and VL staying at the A-W interface are ~72%, ~68%, and ~73%, respectively. As the size of $(TiO_2)_n$ clusters increases, the adsorption capacity decreases until $n > 4$, and beyond this, the capacity remains stable. A-W interface and TiO_2 clusters facilitate Ph and VL reactions initiated by the O_3 and $HO^{\bullet}$, respectively. However, oxidation reactions of 4-HBA are little affected by environmental media because of its electron-withdrawing group. The O_3- and $HO^{\bullet}$-initiated reaction rate constant (k) values follow the order of $A\text{-}W_{Ph} > TiO_{2\ VL} > A\text{-}W_{VL} > A\text{-}W_{4\text{-}HBA} > TiO_{2\ 4\text{-}HBA} > TiO_{2\ Ph}$ and $TiO_{2\ VL} > A\text{-}W_{Ph} > A\text{-}W_{VL} > TiO_{2\ 4\text{-}HBA} > TiO_{2\ Ph} > A\text{-}W_{4\text{-}HBA}$, respectively. Some byproducts are more harmful than their parent compounds, so should be given special attention. This work provides key evidence for the rapid oxidation observed in the $O_3/HO^{\bullet}$ + PhCs experiments at the A-W interface.

45 More importantly, differences in oxidation of PhCs by different

46 environmental media due to the impact of substituent groups were also

47 identified.

48 **Keywords:** Air-water interface; Titanium dioxide (TiO_2); Phenolic

49 Compounds; Adsorption mechanisms; Molecular dynamics (MD).

50 **1. Introduction**

51 Biomass burning, stemming from natural wildfires and human activity,

52 significantly contributes to atmospheric particulate matter (PM). Biomass

53 burning is a primary source of approximately 90% of the global primary

54 organic aerosols (POA) and releases a substantial quantity of organic

55 pollutants (Ito and Penner, 2005; Chen et al., 2017; Chen et al., 2023).

56 Biomass burning is to blame for about 62% of total annual emissions of

57 about 8.0 Tg of black carbon and 93% of total annual emission of about

58 33.9 Tg of organic carbon worldwide (Bond et al., 2004). Emissions from

59 biomass combustion are one of the primary sources of atmospheric and

60 particle pollutants that negatively affect human health, air quality, and

61 climate (Reid et al., 2005; Yao et al., 2016). One of the three main types of

62 biopolymers responsible for the formation of biomass is lignin (Sun et al.,

63 2011), also the polymeric organic molecule most abundant in plants (Lou

64 et al., 2010; Soongprasit et al., 2020). Pyrolysis of lignin releases phenolic

65 compounds (PhCs) into the air, including phenols, phenolic aldehydes, and

66 methoxyphenols. By mass, these PhCs make up between 21% and 45% of

the aerosol composition (Hawthorne et al., 1989; Diehl et al., 2013; Liao et al., 2020; Soongprasit et al., 2020). Methoxyphenols are one of the potential tracers that can be found in atmospheric wood smoke pollution, with the emission rate ranging from 900 to 4200 mg kg^{-1} fuel (Hawthorne et al., 1989; Rogge et al., 1998; Simoneit, 2002; Chen et al., 2017). Evidence shows that the oxidation processes of PhCs can result in the formation of secondary organic aerosol (SOA) (Yee et al., 2013; Jiang et al., 2023). Hence, it is imperative to explore the effects of PhCs when exposed to atmospheric oxidants.

After being released into the atmosphere, PhCs will be oxidized by ozone (O$_3$) and hydroxyl radicals (HO$^{\bullet}$). Both are significant contributors to SOA (Arciva et al., 2022). The homogenous oxidation of PhCs has been the emphasis of previous studies (Henry et al., 2008; Yee et al., 2013; Liu et al., 2019; Arciva et al., 2022). Researchers investigated the kinetics and reaction mechanisms of gas-phase interactions of PhCs with O$_3$ and HO$^{\bullet}$ in the past decade (Kroflič et al., 2018; Smith et al., 2016; Sun et al., 2021a; Sun et al., 2021b; Liu et al., 2022). Furthermore, they investigated the hydroxylation, ring opening, and oligomerization processes of PhCs in the atmospheric liquid phase, with a focus on the potential environmental toxicity and climatic effects of these events (Ma et al., 2021; Liu et al., 2022; Arciva et al., 2022; Carena et al., 2023).

However, there is a dearth of specific data as well as explanations of

the mechanisms involved in the atmospheric oxidation of PhCs at the air-water (A-W) interface. The atmosphere contains a high concentration of aqueous aerosols and water microdroplets (Zhong et al., 2019; Guzman et al., 2022). The oxidation of PhCs can rapidly occur at A-W interface (Rana and Guzman, 2022c). The term "water surface catalysis" denotes the phenomenon where chemical reactions happen at a faster rate at A-W interface compared to the bulk phase (Lee et al., 2015a; Lee et al., 2015b; Yan et al., 2016; Banerjee et al., 2017). In chemical engineering, titanium dioxide (TiO_2) is an essential photoactive component found in atmospheric mineral dust (Sakata et al., 2021; Wang et al., 2023). The interaction between PhCs and TiO_2 is continuous (Grassian, 2009; Rubasinghege et al., 2010; Shang et al., 2021), despite the relatively low prevalence of TiO_2 mineral particles (comprising 0.1% to 10% by mass). Therefore, it is essential to investigate the disparity in the oxidation reaction mechanisms and kinetics of PhCs at A-W interface and mineral dust particles.

Increasing the number of constituents on the aromatic ring would affect the reactivity and lead to complex compounds after reaction addition and/or open ring pathways. Phenol (Ph), 4-hydroxybenzaldehyde (4-HBA), and vanillin (VL) are typical lignin pyrolysis products (Jiang et al., 2010; Kibet et al., 2012) . Thus, we selected Ph, 4-HBA and VL as model compounds to present comprehensive mechanistic information at A-W interface, on TiO_2 clusters, in the gas phase, and in bulk water, using a

combination of molecular dynamics simulation and quantum chemical calculations. Rate constants were calculated throughout a wide temperature range in various EM. Additionally, computational toxicology was employed to evaluate the ecotoxicological impact of PhCs and their transformation products.

2. Methods

2.1 Molecular dynamics simulation

All of the molecular-dynamics simulations were carried out by utilizing the GROMACS 2019 package, which included the AMBER force field. Parametrization of the Ph, 4-HBA, and VL was accomplished by using the GAFF force field in conjunction with RESP charge calculations performed at the M06-2X/6-311++G(3df,2p)//M06-2X/6-31+G(d,p) level. The TIP3P water model was utilized so that individual water molecules may be represented (Jämbeck and Lyubartsev, 2014).

2.1.1 Properties of Ph, 4-HBA, and VL at the A-W interface

Considering the significance of the interfacial behavior of Ph, 4-HBA, and VL at the A-W interface, the properties of these three substances were initially examined by focusing on the A-W interface. **Fig. S1 (a)** depicts a rectangular box that has dimensions of $4 \times 4 \times 9$ nm^3 and has a Z-axis that is perpendicular to the A-W contact. This box was used for all simulations. A water box that is too small may cause the central PhCs molecules to be too close to the interface region, leading to inaccurate results. Conversely,

opting for a water box that is too large can lead to unnecessary waste of computational resources. To begin the process of constructing the initial configurations, a water slab measuring $4 \times 4 \times 4$ nm^3 was positioned at the coordinates (2 nm, 2 nm, 4.5 nm) of the center of mass (COM). Because the rest extension along the Z-axis of the box was sufficiently large (2.5 nm^3), it was possible to steer clear of the intersection of two A-W interface. Prior to the formal simulation, six Ph molecules were randomly selected position placed in a vacuum above the water box for 150 nanoseconds of NVT molecular dynamics simulation. The purpose of simulating 150 ns is to capture the fundamental molecular dynamics that occur on this time scale, such as bond formation, conformational changes, and interaction events. The results show that there are no significant π-π interactions or formation of hydrogen bonds between the Ph molecules. To simplify the model, this was followed by simulations of individual molecules. Ph, 4-HBA, or VL were each placed in their own compartment at the coordinates (2.0 nm, 2.0 nm, 7.75 nm) for each system in order to simulate the behavior of these molecules in the A-W interface region of cloud/fog drops and aerosol liquid water (ALW). To begin, the three different systems were optimized to use the least amount of energy possible. After that, NVT molecular-dynamics simulations were carried out for a total of 150 nanoseconds.

2.1.2 Umbrella sampling simulations

In **Fig. S1 (b)**, the molecule of Ph, 4-HBA, or VL was placed inside the box (their COM is (2.00 nm, 2.00 nm, 6.00 nm)), which is located directly 2.00 nm away from the COM of the water slab. The distance between the COM of Ph, 4-HBA, or VL and that of the water slab was used as the definition for the reaction coordinate (**Fig. S1**). The weighted histogram analysis approach, also known as WHAM, can be used to calculate the free energy profiles of Ph, 4-HBA, or VL when they transition from the gas phase into bulk water (Kumar et al., 1992; Hub et al., 2010) ; details about WHAM are in the Supporting Information **Text S1**.

2.1.3   Radial distribution function

Estimating the strength of hydrogen bonds (HB) between specific atoms can be done with the help of a tool known as the radial distribution function (RDF). **Text S2** has an explanation of the peculiarities of the RDF and the coordination number.

2.2 DFT calculations

In this work, all structural optimization and energy calculation were accomplished by utilizing the Gaussian16 program (Frisch et al., 2016). Calculated at the CCSD(T)/cc-pVDZ, CBS-QB3, B3LYP/6-311+G(d,p), MP2/6-311+G(d,p) and M06-2X/6-311+G(d,p) levels, Cao et al. (Cao et al., 2021) found that M06-2X/6-311++G(3df,2p)//M06-2X/6-31+G(d,p) is reliable for PhCs at gas phase. After analyzing the stability of the wavefunction, the method we used is reliable. Therefore, all calculations

177 for gas-phase reactions are performed at this level. **Text S3** contains a

178 description of the additional calculated details. The frequency correction

179 factor (0.967) has been taken into account. Multiwfn (Lu and Chen, 2012)

180 was used to construct the electron density map. This program integrates

181 Visual Molecular Dynamics (version 1.9.3) (Humphrey et al., 1996) in

182 order to conduct an analysis of the electrostatic potential (ESP) and the

183 average local ionization energy (ALIE).

184 ### *2.3 IRI analysis*

185 Interaction Region Indicator (IRI) (Lu and Chen, 2021) was used to

186 determine the chemical bonds and weak interactions of Ph/4-HBA/VL

187 adsorbed to TiO_2 clusters (the details are in **Text S4**).

188 ### *2.4 Kinetic calculations*

189 **Text S5** contains an explanation of the kinetic calculation methods.

190 ### **3. Result and discussion**

191 ### *3.1 Enrichment of Ph, 4-HBA, and VL at the A-W interface*

192 ### *3.1.1 The uptake of gaseous PhCs at the A-W interface*

193 **Fig. S1** and **Fig. S2** illustrate the relative distributions of water, O_3, and

194 PhCs molecules (Ph, 4-HBA, and VL) in the A-W interface system along

195 the z-axis. HO$^{\bullet}$ are primarily situated at the A-W interface contact, with the

196 potential to diffuse through the water slab interior (Roeselová et al., 2004).

197 **Fig. 1(a)** displays the variation in water density along the Z-coordinate

198 distance from 0 to 9 nm, categorizing three zones: A-W interface (2.25 to

199   2.79 nm and 6.21 to 6.75 nm), air (0 to 2.25 nm and 6.75 to 9 nm), and bulk

200   water (2.79 to 6.21 nm). This method accurately determines the interfacial

201   range (Zhang et al., 2019; Shi et al., 2020). According to location

202   definitions, O_3 percentage distribution was as follows: 26% at the A-W

203   interface; 72% in the air; and 2% in bulk water (**Fig. 1(b)**). **Fig. 1(c)** depicts

204   MD trajectories of Ph diffusion through the water slab from the air region

205   over a 150 ns period. Ph is distributed in the air (8%) and bulk water (20%),

206   with the majority at the A-W interface (72%) (**Fig. 1 (d)**). The majority of

207   4-HBA and VL molecules are located at the A-W interface, constituting 68%

208   and 73% of the total locations as presented in **Fig. S2**.

209   In **Fig. 2(a)**, we observe the three key processes involving PhCs (Ph,

210   4-HBA, or VL) diffusing into the water slab from the air region. (I) The

211   mutual attraction of gaseous Ph, 4-HBA, or VL; (II) The uptake of PhCs

212   (Ph, 4-HBA, or VL) at the A-W interface; (III) The hydration reaction of

213   PhCs (Ph, 4-HBA, or VL) in the bulk water. **Fig. 2(b)** displays the free

214   energy profile of the trajectories as Ph/4-HBA/VL transitions from the air

215   into the bulk water (see **Text 6** for calculations details). The $\Delta G_{gas \rightarrow interface}$

216   values are -0.22 kcal mol^{-1} for the Ph-A-W (Phenol-Air-Water) system,

217   -0.45 kcal mol^{-1} for the A-W$_{4\text{-HBA}}$ (4-hydroxybenzaldehyde at Air-Water)

218   system, and -0.20 mol^{-1} for the A-W$_{VL}$ (Vanillin-Air-Water) system. This

219   finding is consistent with previous studies about Per-and poly-fluoroalkyl

220   substances (PFAS) at A-W interface (Yuan et al., 2023). These values

suggest that it is thermodynamically favorable for PhCs to approach the interfacial water molecules. **Fig. S3** illustrates typical snapshots from the trajectories of PhCs (Ph, 4-HBA, or VL). Initially, one molecule of Ph, 4-HBA, or VL was placed in the center of the water box, with an equivalent COM distance of 2 nm between the PhCs and the air phase. Subsequently, the PhCs moved closer to the interface, leading to adsorption at the A-W interface. During the adsorption process, the H atom of the phenolic hydroxyl group binds to the oxygen atom of the H_2O molecules at the A-W interface, forming H bonds and preventing its return to the bulk water. This property allowed the phenolic hydroxyl groups on PhCs can effectively adhere to the A-W interface, consistent with the experimental observations using steady-state interfacial vibrational spectra (Kusaka et al., 2021) and Fourier transform infrared (FTIR) imaging micro-spectroscopy (Guzman et al., 2022) . Based on these findings, compared to the number of PhCs molecules distributed in the gas phase and in bulk water, the location where air and water meet exhibits an increased the number of PhCs molecules.

3.1.2 *Interface properties of PhCs*

Introducing more hydrophilic functional groups increases the characteristic angle α and β of PhCs at the interface, allowing for more secure adsorption at the water-air interface. The interaction between H_{PhCs} and O_{H_2O} is the primary factor influencing the stability of PhCs at the

243 interface. The coordination number (N) of $H_{Ph-OH}-O_{H_2O}$, $H_{4-HBA-OH}-O_{H_2O}$,

244 and $H_{VL-OH}-O_{H_2O}$ are 2.68, 2.51, and 2.09 respectively. The number of

245 functional groups attached to the benzene ring affects the N value; more

246 functional groups lead to a lower N value. The reason is that aldehyde and

247 methoxy are strong electron-withdrawing groups, which will reduce the

248 conjugation effect between the benzene ring and the hydroxyl group,

249 making the hydrogen atom on the hydroxyl group partially positively

250 charged, thus weakening the hydrogen bonding ability with water

251 molecules. See **Text S7** for interface properties of PhCs.

3.2 Adsorption of Ph, 4-HBA, and VL by TiO$_2$ Clusters

253   The placement of PhCs on TiO$_2$ clusters significantly impacts

254 adsorption energies (Bai et al., 2020). The adsorption capacity of pollutants

255 on cluster surfaces is a key factor influencing degradation efficiency (Qu

256 and Kroes, 2006). The primary mechanism of C atoms adsorption to

257 $(TiO_2)_n$ (n = 1–4) clusters occurs at a range of 2.57 to 2.61 Å and involves

258 interaction between the H_{-OH} atom and the O_{TiO_2} atom, as seen in **Fig. 3(a)**.

259 Hydrogen bonds can be formed between the H_{-OH} atom and the O_{TiO_2} atom

260 (1.80–2.61 Å), improving the adsorption capacity. In contrast, Ph

261 adsorption to $(TiO_2)_n$ (n = 5–6) clusters, ranging from 2.08 to 2.09 Å, is

262 primarily due to interaction between Ti atom and O_{-OH} atom. For a detailed

263 description see **Text S8**.

Adsorption energy a metric of adsorption capacity, is illustrated in **Fig. 3(b)−(d)** for Ph, 4-HBA, and VL on $(TiO_2)_n$ (n = 1–6). TiO_2 exhibits the highest adsorption capacity for Ph. ($\Delta G_{ad} = -72.35$ kcal mol^{-1}) (**Fig. 3(b)**). The adsorption energy values of TiO_2 and $(TiO_2)_3$ for 4-HBA and VL are −45.32 (**Fig. 3(c)**) and −102.46 kcal mol^{-1} (**Fig. 3(d)**), respectively. Physisorption energy range from −1.20 to 9.56 kcal mol^{-1} (Nollet et al., 2003), thus this adsorption process in this study is spontaneous chemical adsorption. However, the capacity of TiO_2 to adsorb VL is significantly higher than that to adsorb Ph and 4-HBA. **Fig. 3(b)−(d)** show that the adsorption capacity falls as the size of TiO_2 clusters increases when n ≤ 4. In contrast, the adsorption capacity remains constant when n > 4. IRI measurements of Ph on the $(TiO_2)_n$ surface (**Fig. 3(e)**) reveal Ph-TiO_2 hydrogen bonds ($H_{Ph}-O_{TiO_2}$ bonds) and their electrostatic and dispersion effects. Benzene C atom of Ph exhibits sp^2 hybridization, meaning it forms one σ-bond and one π-bond. The sp^2 hybridization of benzene for Ph explains its limited interaction with TiO_2 clusters and accounts for the substantial adsorption energy. Similar interactions occur with 4-HBA and VL (**Fig. S7**). Hydrogen bonds form between the H_{-CHO} atom of 4-HBA or VL and the O_{TiO_2} atom, despite the presence of the H_{Ph} atom.

3.3 Continuous oxidation mechanisms

3.3.1 O_3- and HO•-initiated reactions

PhCs, once released into the atmosphere, undergo several processes, including adsorption on mineral aerosol surfaces, accumulation at the A-W interface, dispersion in bulk water within liquid droplets, and oxidation reactions initiated by atmospheric oxidants (Lin et al., 2017) . Reactions inside the aqueous particle have also been a hot topic of interest in recent years (Tilgner et al., 2021; Mabato et al., 2023; Zhang et al., 2024; Rana et al., 2024) , so we also focused on the process by which phenolic compounds enter the interior of the droplet. This section delves into the detailed mechanisms and characteristics of these reactions. At the M06-2X/6-311++G(3df,2p)//M06-2X/6-31+G(d,p) level, the structures with the minimum free energy for the Ph/4-HBA/VL has been determined (**Fig. S10**). In the case of VL, a significant reduction in molecular energy is observed due to the formation of a powerful intramolecular hydrogen bond with a length of 2.09 Å between the H and O atoms near the methyl group. Moreover, the lone pair electrons of oxygen atoms can form additionally p-π conjugations with the π electrons of the phenyl ring, further reducing the overall energy of VL in gas phase. The statistical charts of calculated $\Delta_r G$ and $\Delta G^{\ddagger}$ values for O_3- and $HO^{\bullet}$-initiated reactions are displayed in **Fig. 4** and **S8** and detailed data are available in **Tables 1–4**.

O_3 is a major oxidant in the atmosphere, with high concentrations in the troposphere of 9.85×10^{11} molecules cm $^{-3}$ (Tomas et al., 2003; Pillar-Little et al., 2014). Investigating the fate of PhCs in the presence of O_3 is

307 essential (Pillar-Little et al., 2014; Rana and Guzman, 2020) . The

308 ozonolysis of PhCs involves the synthesis of primary ozonide, the

309 formation of active Criegee intermediate (CI), and the disintegration of CI

310 (Rynjah et al., 2024) . The O_3-initiated reactions of Ph/4-HBA/VL involve

311 radical adduct formation (RAF) channels on their benzene ring ($R_{O_3\text{-RAF}}1-$

312 6), highlighted in red in **Fig. S10**. **Fig. 4(a)−(d)** depict that the ozonolysis

313 pathways $R_{O_3\text{-RAF}}$ are exergonic, indicating their spontaneity. The average

314 $\Delta G^{\ddagger}$ values for the ozonolysis of Ph/4-HBA/VL are ranked as Ph > VL >

315 4-HBA. The following is a list of the average values for the ozonolysis of

316 Ph/4-HBA/VL, as illustrated in **Fig. 4(e)**–**5(h)**, Ph is superior to VL and 4-

317 HBA, with the exception on TiO_2 clusters. **Fig. 4(e)** illustrates that the

318 average value of $\Delta G^{\ddagger}$ for O_3 + Ph reactions at the A-W interface is 15.38

319 kcal mol^{-1}, the lowest value out of the three PhCs. The average $\Delta G^{\ddagger}$ values

320 for the ozonolysis of Ph/4-HBA/VL are as follows: VL (13.95 kcal mol^{-1})

321 < Ph (24.70 kcal mol^{-1}) < 4-HBA (25.16 kcal mol^{-1}) on TiO_2 clusters (**Fig.**

322 **4(f)**). The average $\Delta G^{\ddagger}$ values for O_3 + VL reactions in gas phase are the

323 highest among the four different EM (23.28 kcal mol^{-1}) shown in **Fig.**

324 **4(g)**). Comparing the phenolic oxidation in each of these four EM (bulk

325 water, interface, TiO_2 clusters, and gas phase) reveals that A-W interface

326 are more conducive to the ozonolysis of Ph, whereas TiO_2 clusters are more

327 conducive to the ozonolysis of VL. The effect of solvation on $\Delta G^{\ddagger}$ is

328 predominantly caused by the hydration of the phenolic OH group, as this

329 is the part of the molecule being solvated. However, the presence of water

330 molecules in the region around the phenyl group has been shown to have a

331 considerable influence on the $\Delta G^{\ddagger}$ values.

332   HO$^{\bullet}$, known as "atmospheric detergents", is another significant

333 atmospheric oxidant (Atkinson, 1986; Zhang et al., 2020). The worldwide

334 mean tropospheric concentration of HO$^{\bullet}$ is roughly 11.3×10^{5} molecules

335 cm^{-3} (Lelieveld et al., 2016). For this reason, elucidating the reaction

336 mechanism underlying HO$^{\bullet}$ + PhCs reactions in the troposphere is of the

337 utmost importance. HO$^{\bullet}$-initiated reaction pathways of Ph/4-HBA/VL

338 include RAF, hydrogen atom abstraction (HAA) channels from the

339 benzene ring (R$_{HAA}$ben1–6) and the substituent group (R$_{HAA}$sub7–9).

340 Previous research (Gao et al., 2019) has shown that the process of single

341 electron transfer (SET) does not significantly contribute to the HO$^{\bullet}$-

342 initiated reactions examined. Once the hydroxyl adducts or H$_2$O are formed,

343 significant heats (4.21–30.28 kcal mol^{-1}) are released (**Fig. 4(i)–(l), S8**

344 **(a)–(d) and (i)–(l)**; the detail data in **Table S3**), indicating high

345 thermodynamic feasibility. The average $\Delta G^{\ddagger}$ values for HO$^{\bullet}$-initiated

346 reactions (**Fig. 4(m)–(p), S8 (e)–(h) and (m)–(p)**) are lower than those for

347 O$_3$-initiated reactions. Routs R$_{HAA}$ben make a minimal contribution to HO$^{\bullet}$-

348 initiated reactions. At the A-W interface, VL (3.52 kcal mol^{-1}) < Ph (4.52

349 kcal mol^{-1}) < 4-HBA (9.50 kcal mol^{-1}), and the $\Delta G^{\ddagger}$ value of Ph is the

350 lowest (-0.97 kcal mol^{-1}), the case for pathways R$_{RAF-HO}$$_{\bullet}$ (**Fig.4(m)**).

Among the three aromatic compounds, the $R_{RAF-HO\bullet}$ routes of VL on TiO_2 clusters are most likely to take place (**Fig. 4(n)**). When compared to HO$^\bullet$-initiated reactions of aromatic compounds in the gas phase (**Fig. S9(e)**) or bulk water (**Fig. S9(f)**), the process of Ph + HO$^\bullet$ reactions at the A-W interface is accelerated, whereas the process of VL + HO$^\bullet$ reactions is accelerated by TiO_2 clusters. These findings are in agreement with the ozonolysis findings. The same guidelines can be used to routes R_{HAA}sub (**Fig. 4(o)**, **(p)**, **S8 (g)** and **(h)**) and R_{HAA}ben (**Fig. S8(m)−(p)**). The following is a ranking of the average $\Delta G^{\ddagger}$ values for routes $R_{RAF-HO\bullet}$ in the gas phase or bulk water: Ph < 4-HBA < VL. As a result of having the lowest $\Delta G^{\ddagger}$ values among all HO$^\bullet$-initiated reaction mechanisms, routes R_{RAF} are the most advantageous of all the possible reaction mechanisms. In light of this, each and every route $R_{RAF-HO\bullet}$ and R_{HAA}sub will be dissected in detail.

Fig. 5 shows the $\Delta_r G$ and $\Delta G^{\ddagger}$ values of O_3- and HO$^\bullet$-initiated reactions at various reaction locations. These reactions are almost entirely exothermic, with a close correlation between $\Delta_r G$ values and $\Delta G^{\ddagger}$ values. The $\Delta G^{\ddagger}$ values for the Phe + O_3 reactions shown in **Fig. 5(a)** are the lowest among the three compounds, ranging from −0.97 to 7.86 kcal mol $^{-1}$. Exergonic and spontaneous addition reactions took place at the C1−C2 and C3−C4 locations of Ph and VL, respectively. Because of their low $\Delta G^{\ddagger}$ values, the C1−C2 and C2−C3 sites of O_3-initiated reactions for 4-HBA are advantageous. Their values are 21.76 and 22.03 kcal mol $^{-1}$, respectively.

The C1–C2 location of 4-HBA is activated to a greater extent at the A-W interface in comparison to the gas phase and bulk water. However, the $\Delta G^{\ddagger}$ values of O_3 + Ph reactions on TiO_2 clusters are significantly greater than those of the A-W interface (12.86–18.10 kcal mol^{-1}) than 24.30–25.34 kcal mol^{-1}. The VL + O_3 reactions on TiO_2 clusters are favorable at the C2–C3 and C4–C5 locations (the $\Delta G^{\ddagger}$ values are 11.42 and 11.14 kcal mol^{-1}, respectively, **Fig. 5(b)**). This can be explained by the fact that the electron cloud has a greater propensity to congregate in the places C2–C3 and C4–C5, respectively. In addition, the p orbitals of the methoxy and hydroxy groups are conjugated to the benzene ring, which offers a powerful electron-donating conjugation effect (Aracri et al., 2013). Because of this, the oxidation of aromatic molecules is thermodynamically more favorable than the oxidation of the aldehyde group. This is consistent with previous studies that electron density influences the oxidative activity of PhCs (Rana and Guzman, 2022a). Clearly, the $\Delta G^{\ddagger}$ values of HO$^{\bullet}$-initiated reactions (−0.97~13.46 kcal mol^{-1}) in **Fig. 5(c)−(f)** are lower than those of O_3-initiated processes (11.14~27.83 kcal mol^{-1}) at different points in A-W interface and TiO_2 clusters. This can be seen by comparing the values to each other. At the A-W interface, the most advantageous position for the phenol hydroxyl group to be in for Ph/4-HBA/VL + HO$^{\bullet}$ reactions are the ortho position (**Fig. 5(c)**). OESI-MS, which stands for online electrospray ionization mass spectrometry, was also able to identify the

hydroxylation product known as 3,4-dihydroxybenzaldehyde (Rana and Guzman, 2020). In **Fig. 5(d)**, the ortho- and meta-sites of phenol hydroxyl are, respectively, the most favorable positions for Ph/4-HBA + HO$^{\bullet}$ reactions on the TiO$_2$ clusters. On the other hand, all of the VL sites on the TiO$_2$ clusters are advantageous. At the A-W interface and on the TiO$_2$ clusters, the abstraction of hydrogen atoms follows the order of H$_{-CHO}$ atom > H$_{-OCH_3}$ atom > H$_{-OH}$ atom in **Fig. 5(e) and (f)**. This can also be explained by the ALIE values of these atoms listed in the same order of H$_{-CHO}$ atom (11.67–11.74 eV) > H$_{-OCH_3}$ atom (14.06 eV) > H$_{-OH}$ atom (15.46 eV), as shown in **Fig. S8**.

3.3.2 *Generation and degradation of key products*

For the purposes of this discussion, the primary atmospheric fate of the selected aromatics was considered to be their reactions with O$_2$ (typically mediated by reactive intermediates or catalytic processes) and O$_3$. **Fig. 6** and **S10** illustrate the subsequent reaction mechanisms of IMs, respectively. IM$_{1-2}$ was produced using the pathway that offered the best conditions for the HO$^{\bullet}$-initiated reaction of Ph. As can be seen in **Fig. 6(a)**, the addition of O$_2$ to the C3 sites of the C$_6$H$_5$O radicals results in the formation of C$_6$H$_5$O-OO radicals with no barriers in either the gas phase or the bulk water. This is a desirable outcome. For the transformation of the C$_6$H$_5$O$_2$-OO radicals that were created, the ring closure reaction to form C$_6$H$_5$O$_2$-OO-d is attractive option. However, it must overcome an energy barrier of

18.83 kcal mol $^{-1}$ in the gas phase or 13.67 kcal mol $^{-1}$ in bulk water. The $C_6H_5O_2$-OO-d_1 radical, which was produced by the $C_6H_5O_2$-OO-d reaction, interacts once more with O_2. In the atmosphere, these Criegee intermediates also may undergo bimolecular reactions with NOx (Sun et al., 2020). Malealdehyde (P1) is what should mostly result from the reaction of the $C_6H_5O_2$-OO-d_1 radical with NO. However, during this process, it still needs to overcome an energy barrier of 49.5 (in the gas phase) or 50.83 kcal mol $^{-1}$ (in the bulk water) to generate $C_6H_5O_2$-OO-d_3 radical; as a result, the further transformation of the formed $C_6H_5O_2$-OO-d_2 should continue very slowly. Pyrocatechol (P2) is the primary product generated in the gas phase and bulk water when the H atom of the $C_6H_5O_2$-OO radical is displaced. P2 generates o-semiquinone radicals via pathways R_{HAA} by HO$^\bullet$ or O_3, which in turn generate oligomers (Guzman et al., 2022). This results in the formation of brown organic carbon in atmospheric aerosols. At the A-W interface, a sequence of hydroxylation products, including pyrocatechol (P2), benzene-1,2,3-triol (P3), and benzene-1,2,3,4,5-pentaol (P4), are generated through hydroxylation processes rather than by a single SET ($\Delta G^{\ddagger} = 111.79$ kcal mol $^{-1}$). It is difficult for P4 to form benzene-1,2,3,4,5,6-hexaol because hydrogen transfer reactions are difficult to occur ($\Delta G^{\ddagger} = 34.32$ kcal mol $^{-1}$). These hydroxylation products have been detected by experimental means (Pillar-Little et al., 2014; Pillar-Little and Guzman, 2017; Rana and Guzman, 2020). The HO$^\bullet$

439   abstracts a hydrogen atom from the hydroxyl group of catechol, forming

440    $C_6H_5O_2$ radical and a water molecule. Due to the widespread presence of

441   NO_2 in the environment, it adds to the $C_6H_5O_2$ radical at the ortho position

442   of the extracted hydrogen atom through an addition reaction. Subsequently,

443   a hydrogen transfer reaction occurs, resulting in the formation of 4-

444   nitrobenzene-1,2-diol (P_{2-a}). This computational result validates the

445   previous experimental hypothesis by Finewax et al (Finewax et al., 2018).

446   The P_{2-a} subsequently transform into benzoquinone, maleic acid, fumaric

447   acid, acetic anhydride, acetic acid, and formic acid, or are directly

448   mineralized into carbon dioxide and water (Chen et al., 2015). In order to

449   gain a more comprehensive understanding of the reaction mechanism at

450   the A-W interface, the major product (the $C_7H_5O_2$ radical) for pathways

451   R_{HAA} of 4-HBA was also taken into consideration. According to **Fig. S11**

452   **(a)**, the addition of HO$^{\bullet}$ to the C7 sites of the $C_7H_5O_2$ radical can occur

453   without any obstructions. The overpowering of the 18 kcal mol^{-1} barrier

454   resulted in the formation of the hydroxylation products (4-hydroxybenzoic

455   acid (P5), 3,4-dihydroxybenzoic acid (P6), 2,3,4-trihydroxybenzoic acid

456   (P7), and 2,3,4,5,6-pentahydroxybenzoic acid (P8)). There was found to be

457   one transition route for the continued ozonolysis of the hydroxylation

458   products that were produced in P6. The C2–C3 site of P6 to create P6-5O$_3$

459   ($\Delta G^{\ddagger}$ = 16.59 kcal mol^{-1}) has the lowest activation energy of all the

460   available paths for the relevant reactions (**Fig. S11(b)**). This corresponds

461 to a value of 16.59 kcal mol $^{-1}$. When the $\Delta G^{\ddagger}$ values of the breakage of

462 five-membered rings created by ozonolysis pathways are compared, one

463 can get the conclusion that the formation of IM_{P6}-5O_3-a is the most favored

464 pathway. All of the hydrogen abstraction processes involving H_2O and

465 IM_{P6}-5O_3-a have rather high energy barriers (32.93 kcal mol $^{-1}$). On the

466 other hand, in **Fig. S10(a)**, the very low $\Delta G^{\ddagger}$ values (19.74 ~ 22.89 kcal

467 mol $^{-1}$) of the -NO-O abstraction make it a desirable choice. Following a

468 chain of ozonolysis reactions, the following products were obtained

469 (**Fig.S11(c)**) : ((2E,4Z)-2-formyl-4,5-dihydroxy-6-oxohexa-2,4-dienoic

470 acid (P9); 2,3-dihydroxymalealdehyde (P10); and 2,3-dioxpropanoic acid

471 (P11). Therefore, the product that was created, P10, may also be the

472 product that was discovered through experimentation (mass to charge

473 ratios (m/z) = 115) (Rana and Guzman, 2020). The VL subsequent reaction

474 mechanism is demonstrated in **Fig. S11(d)**. The final oxidation products of

475 VL are P12 ((2E,4E)-4-formyl-2-methoxy-6-oxohexa-2,4-dienoic acid),

476 P13 (ethene-1,1,2-tricarbaldehyde), P14 (2-methoxy-2-oxoacetic acid),

477 P15 (oxalaldehyde) and P16 ((E)-2-methoxy-4,5-dioxopent-2-enoic acid).

478 The formation of these products could explain the biomass burning

479 material for the formation of SOA (Rana and Guzman, 2022b).

480 *3.4 Comparison with available experimental results*

481 The rate constants (*k*) of the overall reaction under the temperature

482 range of 278–318 K were computed based on acquired potential energy

surfaces for the O_3-initiated and HO$^{\bullet}$-initiated reactions of selected

compounds. The results of these calculations are listed in **Table S5** and **S6**,

respectively. The temperature dependences of the various k values for Ph,

4-HBA, and VL at the A-W interface and in bulk water are depicted in **Fig.**

7. At low values of k, there is a positive dependence on temperature. When

the k values are raised to a certain degree, the temperature dependency

seems to lose any significance it may have had before. The following is an

order of the k values for O_3-initiated reactions: A-W$_{Ph}$ > TiO$_2$ $_{VL}$> A-W$_{VL}$ >

A-W$_{4-HBA}$ > TiO$_2$ $_{4-HBA}$ > TiO$_2$ $_{Ph}$ **(Fig. 7(a))**. According to **Fig. 7(b)**, the k

values of HO$^{\bullet}$-initiated reactions go as follows: TiO$_2$ $_{VL}$ > A-W $_{Ph}$ > A-W$_{VL}$>

TiO$_2$ $_{4-HBA}$ > TiO$_2$ $_{Ph}$> A-W$_{4-HBA}$. In **Fig. 7(a)** and **Fig. 7(b)**, the k values of

HO$^{\bullet}$-initiated reactions are one hundred times greater than those of O_3-

initiated reactions. **Table 1** is a listing of the experimental and estimated k

values that are available for O_3-initiated and HO$^{\bullet}$-initiated reactions at 298

K. According to the findings, the ozonolysis of Ph was promoted by the

water-gas interface as well as by TiO$_2$ clusters, and the HO$^{\bullet}$ initiated

reactions of VL were promoted by TiO$_2$ clusters. However, the O_3/HO$^{\bullet}$ +

4-HBA reactions have the lowest k values among the three molecules when

tested in a variety of environmental environments. The estimated k_{O_3+Ph}

values at the A-W interface are 11 orders of magnitude greater than those

of catechol under dry conditions in gas phase (Zein et al., 2015), when

compared with the experimental data. Because it has a higher k_{O_3} value,

catechol, which is one of the main products of Ph's oxidation in the atmosphere, has a higher degree of reactivity than its parent compound (**Table 1**). The estimated value of VL is lower than the experimentally determined value of k_{O_3} for guaiacol under dry conditions, which is $(0.40 \pm 0.31) \times 10^{-18}$ cm^3 molecule^{-1} s^{-1} in the gas phase (Zein et al., 2015). The difference between the predicted value of $k_{HO^\bullet + VL}$ is 1.14×10^{-10} cm^3 molecule^{-1} s^{-1} and the average experimental value of $k_{HO^\bullet}$ for methoxyphenols is just an order of magnitude. As a consequence, the findings of our calculations are reliable. Previous studies measured the second order rate constants of guaiacylacetone $+$ HO$^\bullet$ reaction to be $(14-25) \times 10^9$ M^{-1} s^{-1} at pH 5 and 6 at aqueous secondary organic aerosol, which is lower than our results (Arciva et al., 2022). This is because galactose reduces the steady-state concentration of HO$^\bullet$. The reaction rate constants of PhCs increase with increasing pH and we calculated the rate constants at pH 7 in bulk water (Ma et al., 2021). This study summarizes the O$_3$- and HO$^\bullet$-initiated reaction sequences of three PhCs in different environmental media. The reaction sequences for O$_3$- and HO$^\bullet$-initiated reactions of Ph and 4-HBA are identical in different environmental media, while VL shows slight variations. For O$_3$-initiated reactions, the reaction sequences are as follows: Ph: A-W interface > Bulk water > Gas phase > TiO$_2$ clusters; 4-HBA: Bulk water > A-W interface > TiO$_2$ clusters > Gas phase; VL: Bulk water > TiO$_2$ clusters > A-W interface > Gas phase. For HO$^\bullet$-initiated

reactions, the sequences are: Ph: A-W interface $\approx$ Bulk water > Gas phase > TiO$_2$ clusters; 4-HBA: Bulk water > A-W interface > TiO$_2$ clusters > Gas phase; VL: TiO$_2$ clusters > Bulk water > A-W interface > Gas phase. According to the atmospheric concentration of O$_3$, the atmospheric lifetime of Ph is the shortest (< 1s) of the three PhCs at the gas-water interface or bulk water, whereas 4-HBA and VL were oxidized more slowly than Ph (Smith et al., 2016). See **Fig. S12** and **Text S9** for ecotoxicity assessment.

4. Conclusions

Combining molecular dynamic simulations (with the AMBER force field) and quantum chemical calculations (at the M06–2X/6–311++G(3df,2p)//M06–2X/6-31+G(d,p) level) methods has provided comprehensive insights into the surface properties of Ph, 4-HBA, and VL, as well as their reactions induced by O$_3$ and HO$^\bullet$, both in homogeneous and heterogeneous environments. Here are some key findings from this research:

(1) Free energy well of Ph, 4-HBA, and VL favor the A-W interface as their preferred location, with the occurrence percentages of approximately ~72%, ~68%, and ~73% respectively. Ph and 4-HBA show a preference for the A-W interface over the air, with energy difference of around 0.22 and 0.45 kcal mol $^{-1}$. The VL adsorbed on the TiO$_2$ clusters has a higher likelihood of remaining compared to VL adsorbed at the A-W interface. (2) The adsorption capacity of TiO$_2$ clusters decreases with increasing cluster

size until n > 4. After that point, the adsorption capacity remains constant.

Strong electrostatic attractive interactions and attractive dispersion effects

occur between the benzene of the Ph and Ti atoms. Hydrogen bonds form

between the atom of O_{TiO_2} and the H_{-CHO} group of 4-HBA or VL. (3) The

O_3- and HO$^\bullet$-initiated reactions for Ph and VL are facilitated by the A-W

interface and TiO_2 clusters, respectively, For O_3-initiated reactions at the

A-W interface, the C1–C2 position on the benzene ring is most favorable.

In both the A-W interface and on TiO_2 clusters, the total branching ratio for

routes R_{RAF} and R_{HAA}sub is 72.68% ~ 100%. For route R_{HAA}sub, the order

is H_{-CHO} atom > H_{-OCH_3} atom > H_{-OH} atom. (4) The k values (in

molecules·cm^{-3} s^{-1}, at 298K and 1 atm) of O_3-initiated reactions follow

the order of A-W$_{Ph}$ (5.98×10^{-7}) > TiO_2 $_{VL}$ (3.30×10^{-15}) > A-W$_{VL}$ (1.27

$\times 10^{-17}$) > A-W$_{4\text{-}HBA}$ (6.79×10^{-23}) > TiO_2 $_{4\text{-}HBA}$ (5.32×10^{-24}) > TiO_2 $_{Ph}$

(1.84×10^{-24}). The k values of HO$^\bullet$-initiated reactions follow the order of

TiO_2 $_{VL}$ (6.70×10^{-6}) > A-W$_{Ph}$ (2.69×10^{-6}) > A-W$_{VL}$ (1.73×10^{-7}) > TiO_2

$_{4\text{-}HBA}$ (3.16×10^{-9}) > TiO_2 $_{Ph}$ (3.17×10^{-10}) > A-W$_{4\text{-}HBA}$ (9.49×10^{-11}). (5)

Toxicity risk assessment on aquatic species reveal that most of the reaction

products are significantly less harmful than the parent compounds.

However, products P1, P2, P3, P10, and P11 are more hazardous, and

further investigation of their atmospheric fate is recommended.

Ph undergoes transformation to malealdehyde and catechol when

exposed to O_3 or HO$^\bullet$ in the troposphere (Xu and Wang, 2013). When

Ph/VL is at the droplet aerosol interface, rapid oxidation to polyhydroxylated compounds occurs (Ma et al., 2021). VL eventually creates tiny molecule aldehydes and acids. This is consistent with experimental observations (Rana and Guzman, 2020). This oxidation process is accelerated when VL is encased in a mineral aerosol represented by TiO$_2$ clusters. Li et al. found that seasonal average concentrations of total nitrophenol compounds in particulate matter were comparable to those measured in the gas phase (Li et al., 2022) . However, the reactivity order of nitrophenols in the atmospheric compartments is water droplets > gas phase > particles (Vione et al., 2009). The formation of some low molecular weight acids and aldehydes (2,3-dihydroxymalealdehyde, 2,3-dioxpropanoic acid, etc.) confirms their association with the formation of SOA. It is recommended that enterprises producing lignin, such as those in the pulp and paper industry, or factories that employ lignin in the manufacturing of adhesives, rust inhibitors, color dispersants, diluents, or other similar products, be constructed in regions with low relative humidity. It is recommended that treatment facilities that collect lignin pyrolysis products and recycle the byproducts be located in the surrounding area.

Author contributions

Yanru Huo contributed to the manuscript conceptualization, methodology, software, formal analysis, investigation, and writing of the original manuscript. Mingxue Li provided insight into the writing ideas throughout

the article. Xueyu Wang offered some guidance on the method section of the manuscript. Jianfei Sun, Yuxin Zhou, and Ma Yuhui reviewed the original manuscript. Maoxia He: Conceptualization, Resources, Writing – review & editing, Supervision, Funding acquisition.

Competing interests

The contact author has declared that none of the authors has any competing interests.

Acknowledgements

This work was financially supported by the National Natural Science Foundation of China (NSFC No. 22276109, 21777087, and 21876099).

Reference

Aracri, E., Tzanov, T., and Vidal, T.: Use of Cyclic Voltammetry as an Effective Tool for Selecting Efficient Enhancers for Oxidative Bioprocesses: Importance of pH, Ind Eng Chem Res, 52, 1455-1463, https://doi.org/10.1021/ie3027586, 2013.

Arciva, S., Niedek, C., Mavis, C., Yoon, M., Sanchez, M. E., Zhang, Q., and Anastasio, C.: Aqueous ·OH Oxidation of Highly Substituted Phenols as a Source of Secondary Organic Aerosol, Environ. Sci. Technol., 56, 9959-9967, https://doi.org/10.1021/acs.est.2c02225, 2022.

Atkinson, R.: Kinetics and mechanisms of the gas-phase reactions of the hydroxyl radical with organic compounds under atmospheric

conditions, Chem. Rev, 86, 69-201, https://doi.org/10.1021/cr00071a004, 1986.

Bai, F.-Y., Ni, S., Ren, Y., Tang, Y.-Z., Zhao, Z., and Pan, X.-M.: DFT analysis on the removal of dimethylbenzoquinones in atmosphere and water environments: ·OH-initiated oxidation and captured by (TiO2)n clusters (n=1–6), J Haz Mat, 386, 121636, https://doi.org/10.1016/j.jhazmat.2019.121636, 2020.

Banerjee, S., Gnanamani, E., Yan, X., and Zare, R. N.: Can all bulk-phase reactions be accelerated in microdroplets?, Analyst, 142, 1399-1402, https://doi.org/10.1039/C6AN02225A, 2017.

Bond, T. C., Streets, D. G., Yarber, K. F., Nelson, S. M., Woo, J.-H., and Klimont, Z.: A technology-based global inventory of black and organic carbon emissions from combustion, J Geophys Res-Atoms, 109, https://doi.org/10.1029/2003JD003697, 2004.

Cao, H., Wang, K., Yang, Z., Wu, S., and Han, D.: Quantum chemical study on the ozonolysis mechanism of guaiacol and the structure-reactivity relationship of phenols with hydroxyl, methoxy, and methyl substituents, Chem. Eng. J., 420, 127629, https://doi.org/10.1016/j.cej.2020.127629, 2021.

Carena, L., Zoppi, B., Sordello, F., Fabbri, D., Minella, M., and Minero, C.: Phototransformation of Vanillin in Artificial Snow by Direct Photolysis and Mediated by Nitrite, Environ. Sci. Technol.,

https://doi.org/10.1021/acs.est.3c01931, 2023.

Chen, C., Chen, H., Yu, J., Han, C., Yan, G., and Guo, S.: p-Nitrophenol Removal by Bauxite Ore Assisted Ozonation and its Catalytic Potential, CLEAN – Soil, Air, Water, 43, 1010-1017, https://doi.org/10.1002/clen.201400330, 2015.

Chen, J., Li, C., Ristovski, Z., Milic, A., Gu, Y., Islam, M. S., Wang, S., Hao, J., Zhang, H., and He, C.: A review of biomass burning: Emissions and impacts on air quality, health and climate in China, Sci Total Environ, https://doi.org/10.1016/j.scitotenv.2016.11.025, 2017.

Chen, P., Li, Y., Zhang, Y., Xue, C., Hopke, P. K., and Li, X.: Dynamic Changes of Composition of Particulate Matter Emissions during Residential Biomass Combustion, Environ. Sci. Technol., 57, 15193-15202, https://doi.org/10.1021/acs.est.3c05412, 2023.

Diehl, B. G., Brown, N. R., Frantz, C. W., Lumadue, M. R., and Cannon, F.: Effects of pyrolysis temperature on the chemical composition of refined softwood and hardwood lignins, Carbon, 60, 531-537, https://doi.org/10.1016/j.carbon.2013.04.087, 2013.

Finewax, Z., de Gouw, J. A., and Ziemann, P. J.: Identification and Quantification of 4-Nitrocatechol Formed from OH and NO_3 Radical-Initiated Reactions of Catechol in Air in the Presence of NOx: Implications for Secondary Organic Aerosol Formation from Biomass Burning, Environ. Sci. Technol., 52, 1981-1989,

659   https://doi.org/10.1021/acs.est.7b05864, 2018.

660 Frisch, M. J., Trucks, G. W., Schlegel, H. B., Scuseria, G. E., Robb, M. A.,

661   Cheeseman, J. R., Scalmani, G., Barone, V., Petersson, G. A., Nakatsuji,

662   H., Li, X., Caricato, M., Marenich, A. V., Bloino, J., Janesko, B. G.,

663   Gomperts, R., Mennucci, B., Hratchian, H. P., Ortiz, J. V., Izmaylov, A.

664   F., Sonnenberg, J. L., Williams, Ding, F., Lipparini, F., Egidi, F., Goings,

665   J., Peng, B., Petrone, A., Henderson, T., Ranasinghe, D., Zakrzewski,

666   V. G., Gao, J., Rega, N., Zheng, G., Liang, W., Hada, M., Ehara, M.,

667   Toyota, K., Fukuda, R., Hasegawa, J., Ishida, M., Nakajima, T., Honda,

668   Y., Kitao, O., Nakai, H., Vreven, T., Throssell, K., Montgomery Jr., J.

669   A., Peralta, J. E., Ogliaro, F., Bearpark, M. J., Heyd, J. J., Brothers, E.

670   N., Kudin, K. N., Staroverov, V. N., Keith, T. A., Kobayashi, R.,

671   Normand, J., Raghavachari, K., Rendell, A. P., Burant, J. C., Iyengar,

672   S. S., Tomasi, J., Cossi, M., Millam, J. M., Klene, M., Adamo, C.,

673   Cammi, R., Ochterski, J. W., Martin, R. L., Morokuma, K., Farkas, O.,

674   Foresman, J. B., and Fox, D. J.: Gaussian 16 Rev. C.01 [code], 2016.

675 Gao, Y., Li, G., Qin, Y., Ji, Y., Mai, B., and An, T.: New theoretical insight

676   into indirect photochemical transformation of fragrance nitro-musks:

677   Mechanisms, eco-toxicity and health effects, Environ Int, 129, 68-75,

678   https://doi.org/10.1016/j.envint.2019.05.020, 2019.

679 Grassian, V. H.: New Directions: Nanodust – A source of metals in the

680   atmospheric   environment?,   Atmos   Environ,   43,   4666-4667,

https://doi.org/10.1016/j.atmosenv.2009.06.032, 2009.

Guzman, M. I., Pillar-Little, E. A., and Eugene, A. J.: Interfacial Oxidative Oligomerization of Catechol, ACS Omega, 7, 36009-36016, https://doi.org/10.1021/acsomega.2c05290, 2022.

Hawthorne, S. B., Krieger, M. S., Miller, D. J., and Mathiason, M. B.: Collection and quantitation of methoxylated phenol tracers for atmospheric pollution from residential wood stoves, Environ. Sci. Technol., 23, 470-475, https://doi.org/10.1021/es00181a013, 1989.

Henry, F., Coeur-Tourneur, C., Ledoux, F., Tomas, A., and Menu, D.: Secondary organic aerosol formation from the gas phase reaction of hydroxyl radicals with m-, o- and p-cresol, Atmos Environ, 42, 3035-3045, https://doi.org/10.1016/j.atmosenv.2007.12.043, 2008.

Hub, J. S., de Groot, B. L., and van der Spoel, D.: g_wham—A Free Weighted Histogram Analysis Implementation Including Robust Error and Autocorrelation Estimates, J. Chem. Theory Comput., 6, 3713-3720, https://doi.org/10.1021/ct100494z, 2010.

Humphrey, W., Dalke, A., and Schulten, K.: VMD: Visual molecular dynamics, J Mol Graph Model, 14, 33-38, https://doi.org/10.1016/0263-7855(96)00018-5, 1996.

Ito, A. and Penner, J. E.: Historical emissions of carbonaceous aerosols from biomass and fossil fuel burning for the period 1870–2000, Global Biogeochem Cy, 19, https://doi.org/10.1029/2004GB002374, 2005.

Jämbeck, J. P. and Lyubartsev, A. P.: Update to the general amber force field for small solutes with an emphasis on free energies of hydration, J Phys Chem B, 118, 3793-3804, https://doi.org/10.1021/jp4111234, 2014.

Jiang, G., Nowakowski, D. J., and Bridgwater, A. V.: Effect of the Temperature on the Composition of Lignin Pyrolysis Products, Energ Fuel, 24, 4470-4475, https://doi.org/10.1021/ef100363c, 2010.

Jiang, W., Niedek, C., Anastasio, C., and Zhang, Q.: Photoaging of phenolic secondary organic aerosol in the aqueous phase: evolution of chemical and optical properties and effects of oxidants, Atmos. Chem. Phys., 23, 7103-7120, https://doi.org/10.5194/acp-23-7103-2023, 2023.

Kibet, J., Khachatryan, L., and Dellinger, B.: Molecular Products and Radicals from Pyrolysis of Lignin, Environ. Sci. Technol., 46, 12994-13001, https://doi.org/10.1021/es302942c, 2012.

Kroflič, A., Huš, M., Grilc, M., and Grgić, I.: Underappreciated and Complex Role of Nitrous Acid in Aromatic Nitration under Mild Environmental Conditions: The Case of Activated Methoxyphenols, Environ. Sci. Technol., 52, 13756-13765, https://doi.org/10.1021/acs.est.8b01903, 2018.

Kumar, S., Rosenberg, J. M., Bouzida, D., Swendsen, R. H., and Kollman, P. A.: THE weighted histogram analysis method for free-energy calculations on biomolecules. I. The method, J Comput Chem, 13,

1011-1021, https://doi.org/10.1002/jcc.540130812, 1992.

Kusaka, R., Nihonyanagi, S., and Tahara, T.: The photochemical reaction of phenol becomes ultrafast at the air–water interface, Nat Chem, 13, 306-311, https://doi.org/10.1038/s41557-020-00619-5, 2021.

Lee, J. K., Banerjee, S., Nam, H. G., and Zare, R. N.: Acceleration of reaction in charged microdroplets, Q. Rev. Biophys., 48, 437-444, https://doi.org/10.1017/S0033583515000086, 2015a.

Lee, J. K., Kim, S., Nam, H. G., and Zare, R. N.: Microdroplet fusion mass spectrometry for fast reaction kinetics, PANS, 112, 3898-3903, https://doi.org/10.1073/pnas.1503689112, 2015b.

Lelieveld, J., Gromov, S., Pozzer, A., and Taraborrelli, D.: Global tropospheric hydroxyl distribution, budget and reactivity, Atmos. Chem. Phys., 16, 12477-12493, https://doi.org/10.5194/acp-16-12477-2016, 2016.

Li, M., Wang, X., Zhao, Y., Du, P., Li, H., Li, J., Shen, H., Liu, Z., Jiang, Y., Chen, J., Bi, Y., Zhao, Y., Xue, L., Wang, Y., Chen, J., and Wang, W.: Atmospheric Nitrated Phenolic Compounds in Particle, Gaseous, and Aqueous Phases During Cloud Events at a Mountain Site in North China: Distribution Characteristics and Aqueous-Phase Formation, J Geophys Res-Atoms, 127, e2022JD037130, https://doi.org/10.1029/2022JD037130, 2022.

Liao, Y., Koelewijn, S.-F., Van den Bossche, G., Van Aelst, J., Van den

Bosch, S., Renders, T., Navare, K., Nicolaï, T., Van Aelst, K., Maesen, M., Matsushima, H., Thevelein, J. M., Van Acker, K., Lagrain, B., Verboekend, D., and Sels, B. F.: A Sustainable Wood Biorefinery for Low-Carbon Footprint Chemicals Production, Science, 367, 1385-1390, https://doi.org/10.1126/science.aau1567, 2020.

Lin, P.-C., Wu, Z.-H., Chen, M.-S., Li, Y.-L., Chen, W.-R., Huang, T.-P., Lee, Y.-Y., and Wang, C. C.: Interfacial Solvation and Surface pH of Phenol and Dihydroxybenzene Aqueous Nanoaerosols Unveiled by Aerosol VUV Photoelectron Spectroscopy, J Phys Chem B, 121, 1054-1067, https://doi.org/10.1021/acs.jpcb.6b10201, 2017.

Liu, C., Chen, D., and Chen, X. e.: Atmospheric Reactivity of Methoxyphenols: A Review, Environ. Sci. Technol., 56, 2897-2916, https://doi.org/10.1021/acs.est.1c06535, 2022.

Liu, C., Liu, J., Liu, Y., Chen, T., and He, H. J. A. e.: Secondary organic aerosol formation from the OH-initiated oxidation of guaiacol under different experimental conditions, Atmos Environ, 207, 30-37, https://doi.org/10.1016/j.atmosenv.2019.03.021, 2019.

Lou, R., Wu, S.-b., and Lv, G.-j.: Effect of conditions on fast pyrolysis of bamboo lignin, J Anal Appl Pyrol, 89, 191-196, https://doi.org/10.1016/j.jaap.2010.08.007, 2010.

Lu, T. and Chen, F.: Multiwfn: A multifunctional wavefunction analyzer, J Comput Chem, 33, 580-592, https://doi.org/10.1002/jcc.22885, 2012.

Lu, T. and Chen, Q.: Interaction Region Indicator: A Simple Real Space Function Clearly Revealing Both Chemical Bonds and Weak Interactions**, Chemistry–Methods, 1, 231-239, https://doi.org/10.1002/cmtd.202100007, 2021.

Ma, L., Guzman, C., Niedek, C., Tran, T., Zhang, Q., and Anastasio, C.: Kinetics and Mass Yields of Aqueous Secondary Organic Aerosol from Highly Substituted Phenols Reacting with a Triplet Excited State, Environ. Sci. Technol., 55, 5772-5781, https://doi.org/10.1021/acs.est.1c00575, 2021.

Nollet, H., Roels, M., Lutgen, P., Van der Meeren, P., and Verstraete, W.: Removal of PCBs from wastewater using fly ash, Chemosphere, 53, 655-665, https://doi.org/10.1016/S0045-6535(03)00517-4, 2003.

Pillar-Little, E. A. and Guzman, M. I.: Oxidation of Substituted Catechols at the Air–Water Interface: Production of Carboxylic Acids, Quinones, and Polyphenols, Environ. Sci. Technol., 51, 4951-4959, https://doi.org/10.1021/acs.est.7b00232, 2017.

Pillar-Little, E. A., Camm, R. C., and Guzman, M. I.: Catechol Oxidation by Ozone and Hydroxyl Radicals at the Air–Water Interface, Environ. Sci. Technol., 48, 14352-14360, https://doi.org/10.1021/es504094x, 2014.

Qu, Z.-w. and Kroes, G.-J.: Theoretical Study of the Electronic Structure and Stability of Titanium Dioxide Clusters $(TiO_2)_n$ with $n = 1-9$, J Phys

Chem B, 110, 8998-9007, https://doi.org/10.1021/jp056607p, 2006.

Rana, M. S. and Guzman, M. I.: Oxidation of Phenolic Aldehydes by Ozone and Hydroxyl Radicals at the Air–Water Interface, J Phys Chem A, 124, 8822-8833, https://doi.org/10.1021/acs.jpca.0c05944, 2020.

Rana, M. S. and Guzman, M. I.: Oxidation of Phenolic Aldehydes by Ozone and Hydroxyl Radicals at the Air–Solid Interface, Acs Earth Space Chem, 6, 2900-2909, https://doi.org/10.1021/acsearthspacechem.2c00206, 2022a.

Rana, M. S. and Guzman, M. I.: Surface Oxidation of Phenolic Aldehydes: Fragmentation, Functionalization, and Coupling Reactions, J Phys Chem A, 126, 6502-6516, https://doi.org/10.1021/acs.jpca.2c04963, 2022b.

Rana, M. S. and Guzman, M. I.: Oxidation of Catechols at the Air–Water Interface by Nitrate Radicals, Environ. Sci. Technol., 56, 15437-15448, https://doi.org/10.1021/acs.est.2c05640, 2022c.

Reid, J. S., Eck, T. F., Christopher, S. A., Koppman, R., Dubovik, O., Eleuterio, D. P., Holben, B. N., Reid, E. A., and Zhang, J.: A review of biomass burning emissions part III: Intensive optical properties of biomass burning particles, Atmos. Chem. Phys., 5, 827-849, https://doi.org/10.5194/acp-5-827-2005, 2005.

Roeselová, M., Vieceli, J., Dang, L. X., Garrett, B. C., and Tobias, D. J.: Hydroxyl Radical at the Air−Water Interface, J. Am. Chem. Soc., 126,

16308-16309, https://doi.org/10.1021/ja045552m, 2004.

Rogge, W. F., Hildemann, L. M., Mazurek, M. A., and Cass, G. R.: Sources of Fine Organic Aerosol. 9. Pine, Oak, and Synthetic Log Combustion in Residential Fireplaces, Environ. Sci. Technol., 32, 13-22, https://doi.org/10.1021/es960930b, 1998.

Rubasinghege, G., Elzey, S., Baltrusaitis, J., Jayaweera, P. M., and Grassian, V. H.: Reactions on Atmospheric Dust Particles: Surface Photochemistry and Size-Dependent Nanoscale Redox Chemistry, J. Phys. Chem. Lett., 1, 1729-1737, https://doi.org/10.1021/jz100371d, 2010.

Rynjah, S., Baro, B., and Sarkar, B.: Oxepin Derivatives Formation from Gas-Phase Catechol Ozonolysis, J Phys Chem A, 128, 251-260, https://doi.org/10.1021/acs.jpca.3c04582, 2024.

Sakata, K., Takahashi, Y., Takano, S., Matsuki, A., Sakaguchi, A., and Tanimoto, H.: First X-ray Spectroscopic Observations of Atmospheric Titanium Species: Size Dependence and the Emission Source, Environ. Sci. Technol., 55, 10975-10986, https://doi.org/10.1021/acs.est.1c02000, 2021.

Shang, H., Wang, X., Li, H., Li, M., Mao, C., Xing, P., Zhao, S., Chen, Z., Sun, J., Ai, Z., and Zhang, L.: Oxygen vacancies promote sulfur species accumulation on TiO_2 mineral particles, Appl. Catal. B Environ., 290, 120024, https://doi.org/10.1016/j.apcatb.2021.120024, 2021.

Shi, Q., Zhang, W., Ji, Y., Wang, J., Qin, D., Chen, J., Gao, Y., Li, G., and An, T.: Enhanced uptake of glyoxal at the acidic nanoparticle interface: implications for secondary organic aerosol formation, Environ Sci-Nano, 7, 1126-1135, https://doi.org/10.1039/D0EN00016G, 2020.

Simoneit, B. R. T.: Biomass burning — a review of organic tracers for smoke from incomplete combustion, Appl Geochem, 17, 129-162, https://doi.org/10.1016/S0883-2927(01)00061-0, 2002.

Smith, J. D., Kinney, H., and Anastasio, C.: Phenolic carbonyls undergo rapid aqueous photodegradation to form low-volatility, light-absorbing products, Atmos Environ, 126, 36-44, https://doi.org/10.1016/j.atmosenv.2015.11.035, 2016.

Soongprasit, K., Sricharoenchaikul, V., and Atong, D.: Phenol-derived products from fast pyrolysis of organosolv lignin, Energy Rep, 6, 151-167, https://doi.org/10.1016/j.egyr.2020.08.040, 2020.

Sun, J., Han, D., Shallcross, D. E., Cao, H., Wei, B., Mei, Q., Xie, J., Zhan, J., and He, M.: Theoretical studies on the heterogeneous ozonolysis of syringol on graphene: Mechanism, kinetics and ecotoxicity assessment, Chem. Eng.J., 404, 126484, https://doi.org/10.1016/j.cej.2020.126484, 2021a.

Sun, N., Rodríguez, H., Rahman, M., and Rogers, R. D.: Where are ionic liquid strategies most suited in the pursuit of chemicals and energy from lignocellulosic biomass?, Chem. Commun., 47, 1405-1421,

https://doi.org/10.1039/C0CC03990J, 2011.

Sun, Y., Chen, X., Xu, F., and Wang, X.: Quantum chemical calculations on the mechanism and kinetics of ozone-initiated removal of p-coumaryl alcohol in the atmosphere, Chemosphere, 253, 126744, https://doi.org/10.1016/j.chemosphere.2020.126744, 2020.

Sun, Y., Chen, X., Liu, L., Xu, F., and Zhang, X.: Mechanisms and kinetics studies of the atmospheric oxidation of eugenol by hydroxyl radicals and ozone molecules, Sci Total Environ, 770, 145203, https://doi.org/10.1016/j.scitotenv.2021.145203, 2021b.

Tomas, A., Olariu, R. I., Barnes, I., and Becker, K. H. J. I. J. o. C. K.: Kinetics of the reaction of O_3 with selected benzenediols, 35, 223-230, https://doi.org/10.1002/kin.10121, 2003.

Vione, D., Maurino, V., Minero, C., Duncianu, M., Olariu, R.-I., Arsene, C., Sarakha, M., and Mailhot, G.: Assessing the transformation kinetics of 2- and 4-nitrophenol in the atmospheric aqueous phase. Implications for the distribution of both nitroisomers in the atmosphere, Atmos Environ, 43, 2321-2327, https://doi.org/10.1016/j.atmosenv.2009.01.025, 2009.

Wang, R., Li, K., Li, J., Tsona, N. T., Wang, W., and Du, L.: Interaction of Acrylic Acid and SO2 on the Surface of Mineral Dust Aerosol, Acs Earth Space Chem, 7, 548-558, https://doi.org/10.1021/acsearthspacechem.2c00323, 2023.

Xu, C. and Wang, L.: Atmospheric Oxidation Mechanism of Phenol Initiated by OH Radical, J Phys Chem A, 117, 2358-2364, https://doi.org/10.1021/jp308856b, 2013.

Yan, X., Bain, R. M., and Cooks, R. G.: Organic Reactions in Microdroplets: Reaction Acceleration Revealed by Mass Spectrometry, Angew. Chem. Int. Ed., 55, 12960-12972, https://doi.org/10.1002/anie.201602270, 2016.

Yao, L., Yang, L., Chen, J., Wang, X., Xue, L., Li, W., Sui, X., Wen, L., Chi, J., Zhu, Y., Zhang, J., Xu, C., Zhu, T., and Wang, W.: Characteristics of carbonaceous aerosols: Impact of biomass burning and secondary formation in summertime in a rural area of the North China Plain, Sci Total Environ, 557-558, 520-530, https://doi.org/10.1016/j.scitotenv.2016.03.111, 2016.

Yee, L. D., Kautzman, K. E., Loza, C. L., Schilling, K. A., Coggon, M. M., Chhabra, P. S., Chan, M. N., Chan, A. W. H., Hersey, S. P., Crounse, J. D., Wennberg, P. O., Flagan, R. C., and Seinfeld, J. H.: Secondary organic aerosol formation from biomass burning intermediates: Phenol and methoxyphenols, Atmos. Chem. Phys., 13, 8019-8043, https://doi.org/10.5194/acp-13-8019-2013, 2013.

Yuan, S., Wang, X., Jiang, Z., Zhang, H., and Yuan, S.: Contribution of air-water interface in removing PFAS from drinking water: Adsorption, stability, interaction and machine learning studies, Water Res, 236,

119947, https://doi.org/10.1016/j.watres.2023.119947, 2023.

Zein, A. E., Coeur, C., Obeid, E., Lauraguais, A., and Fagniez, T.: Reaction Kinetics of Catechol (1,2-Benzenediol) and Guaiacol (2-Methoxyphenol) with Ozone, J Phys Chem A, 119, 6759-6765, https://doi.org/10.1021/acs.jpca.5b00174, 2015.

Zhang, W., Ji, Y., Li, G., Shi, Q., and An, T.: The heterogeneous reaction of dimethylamine/ammonia with sulfuric acid to promote the growth of atmospheric nanoparticles, Environ Sci-Nano, 6, 2767-2776, https://doi.org/10.1039/C9EN00619B, 2019.

Zhang, W., Tong, S., Jia, C., Wang, L., Liu, B., Tang, G., Ji, D., Hu, B., Liu, Z., Li, W., Wang, Z., Liu, Y., Wang, Y., and Ge, M.: Different HONO Sources for Three Layers at the Urban Area of Beijing, Environ. Sci. Technol., 54, 12870-12880, https://doi.org/10.1021/acs.est.0c02146, 2020.

Zhong, J., Kumar, M., Anglada, J. M., Martins-Costa, M. T. C., Ruiz-Lopez, M. F., Zeng, X. C., and Francisco, J. S.: Atmospheric Spectroscopy and Photochemistry at Environmental Water Interfaces, Annu Rev Phys Chem, 70, 45-69, https://doi.org/10.1146/annurev-physchem-042018-052311, 2019.
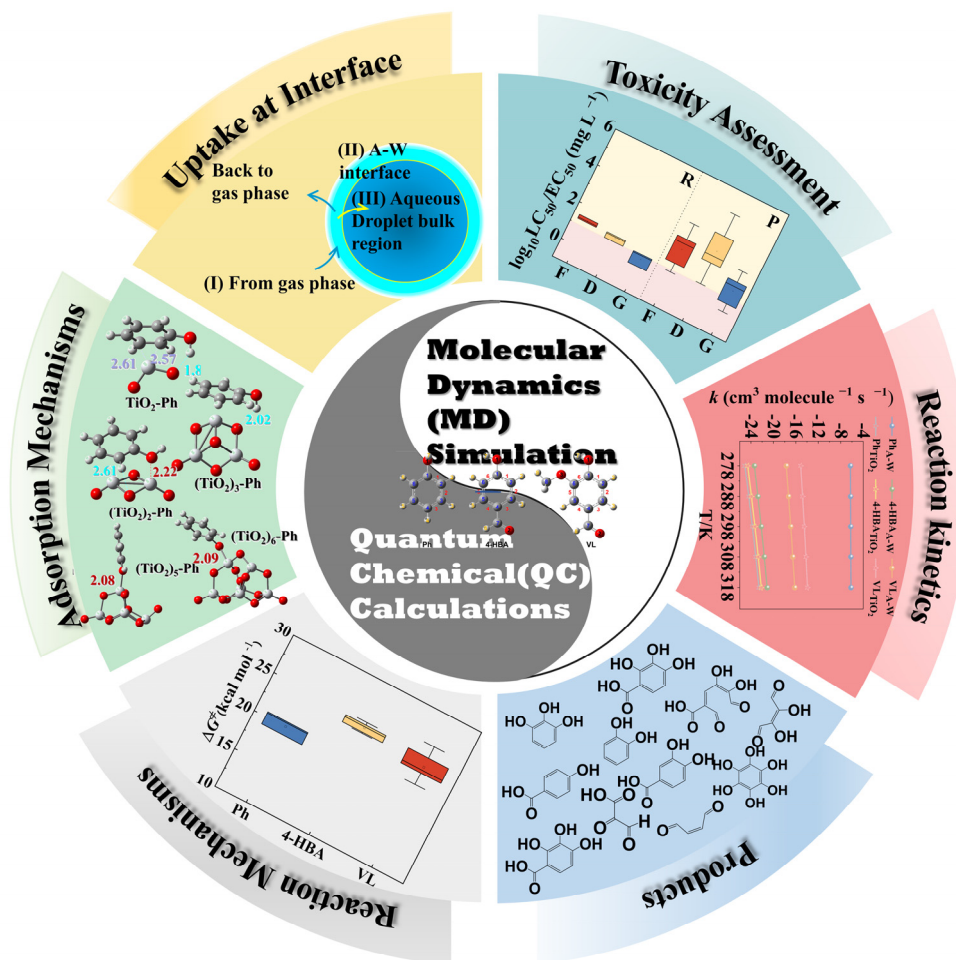
Graphical Abstract
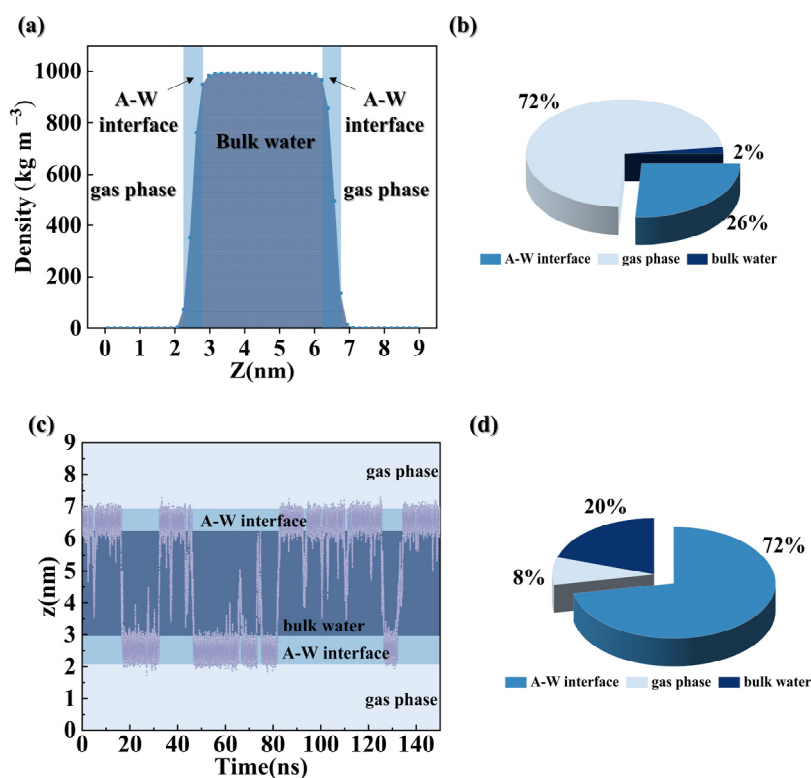
Fig.1 (a) Relative concentration distributions in the A-W system along the z-axis; **(b)** probability of

O_3 at the A-W interface, in gas phase, and in bulk water; **(c)** MD trajectories of Ph diffusion through

the water slab over a 150 ns period; **(d)** probability of Ph at the A-W interface, in gas phase, and in
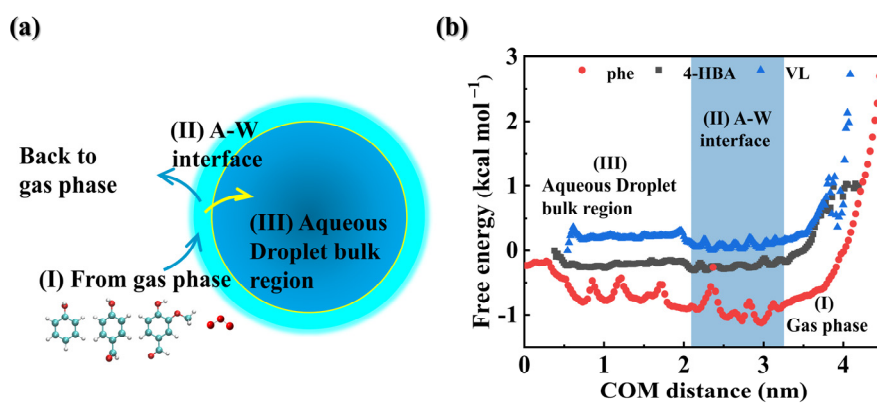
bulk water.

Fig.2 (a) Three key processes for the reaction of gaseous PhCs (Ph, 4-HBA, or VL) with the water

drops; **(b)** free energy change profile of gaseous PhCs (Ph, 4-HBA, or VL) approaching the bulk

water.
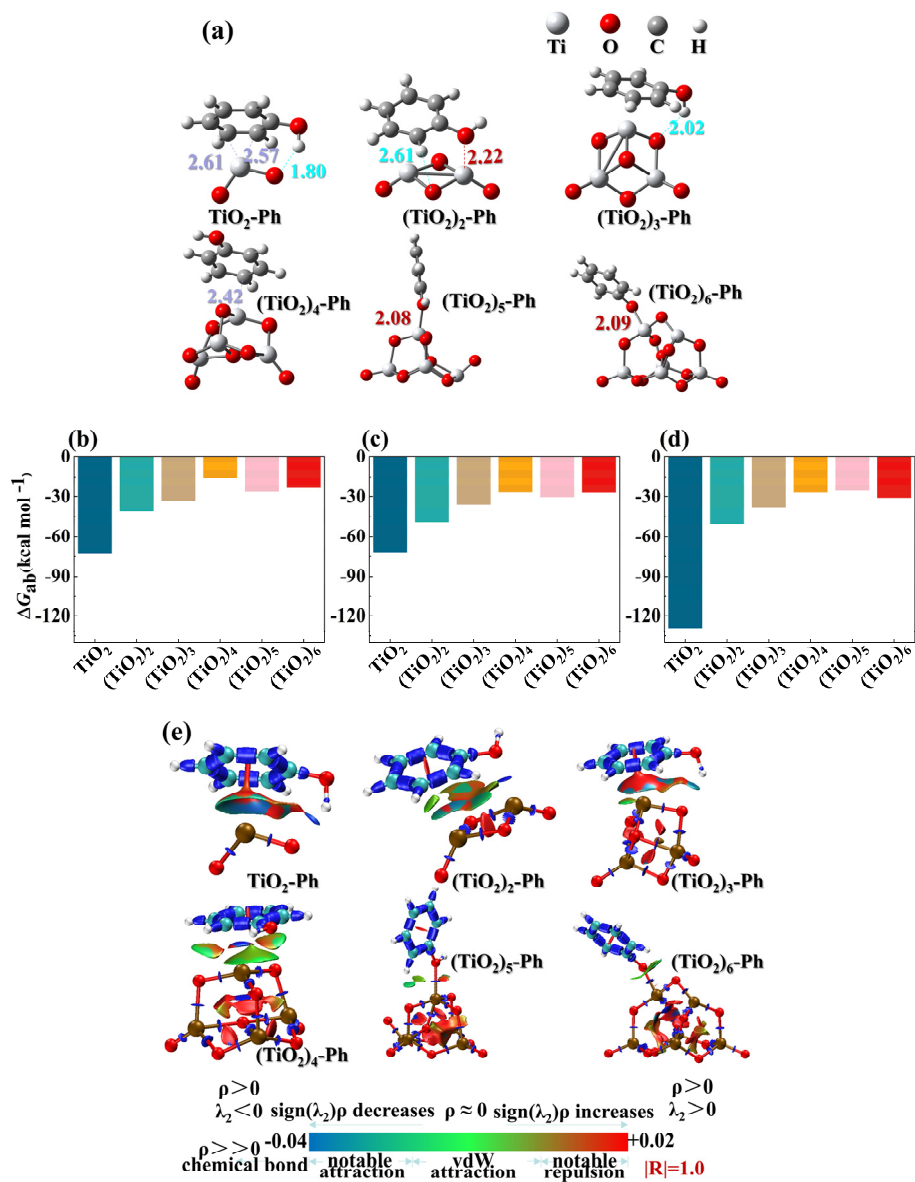
Fig. 3 Adsorption details of PhCs on (TiO$_2$)$_n$ (n = 1−6) clusters; **(a)** structure of Ph adsorption on

(TiO$_2$)$_n$ (n = 1−6) surface; adsorption energy of **(b)** Ph, **(c)** 4-HBA, and (d) VL on (TiO$_2$)$_n$ (n = 1−6,

unit: kcal mol^{-1}); **(e)** Interaction region indicator (IRI) analyses of Ph on (TiO$_2$)$_n$ (n = 1−6) surface.
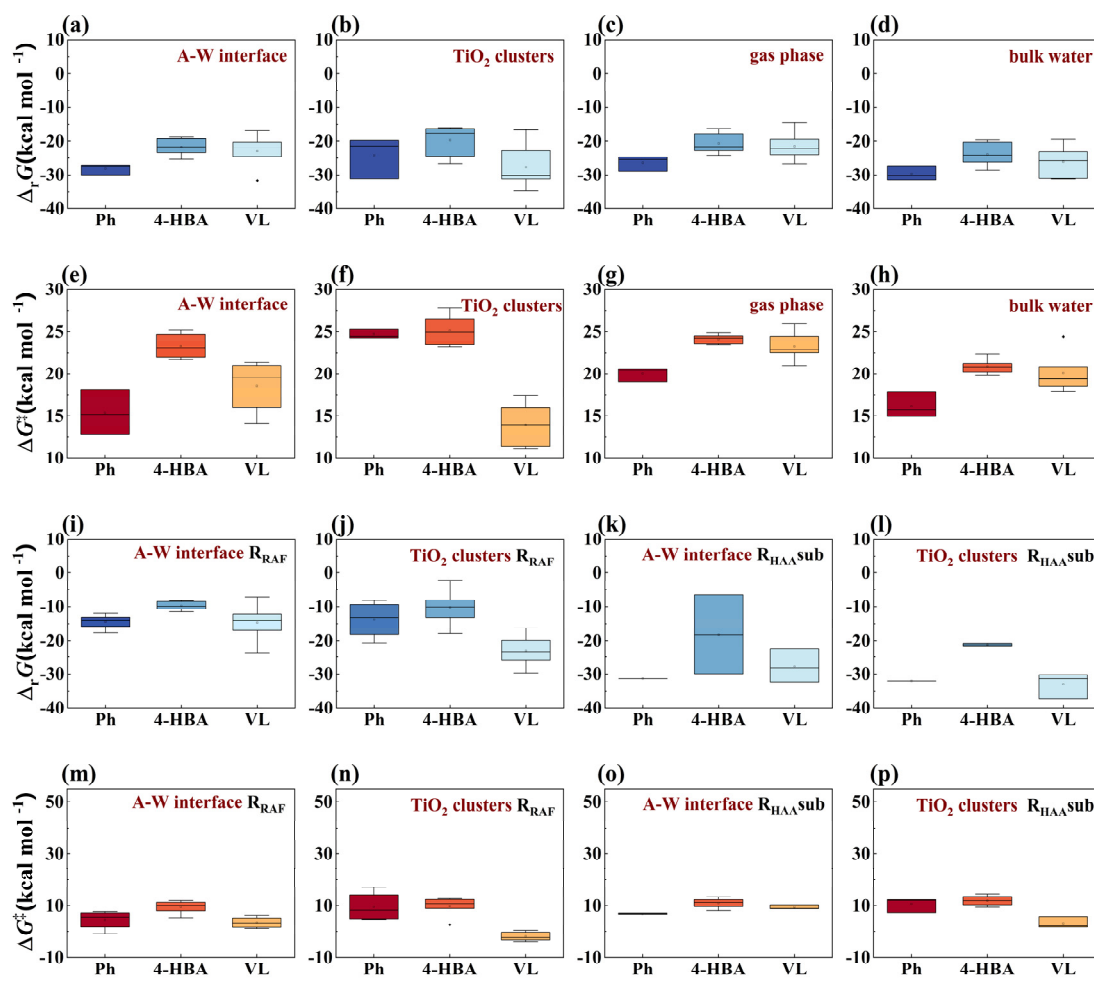
Fig. 4 Statistical charts of calculated **(a)**–**(d)** $\Delta_r G$ and **(e)**–**(h)** $\Delta G^{\ddagger}$ values for O_3-initiated reactions;

(i)–**(l)** $\Delta_r G$ and **(m)**–**(p)** $\Delta G^{\ddagger}$ values for $HO^{\bullet}$-initiated reactions.
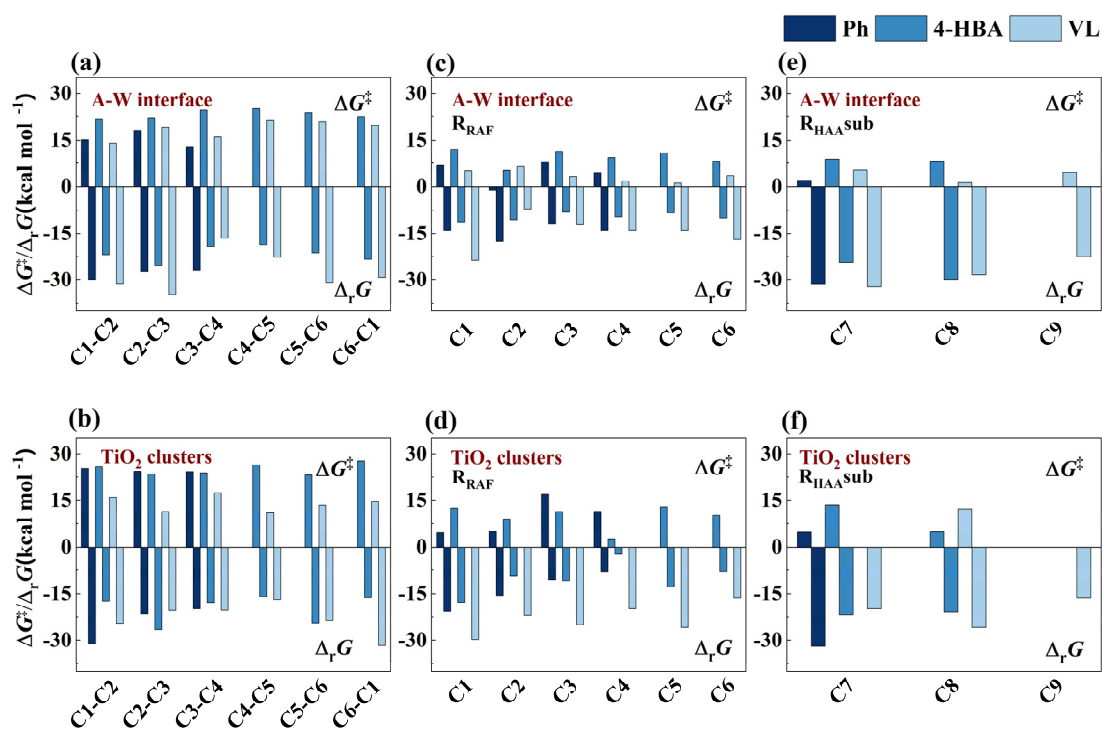
Fig.5 $\Delta_r G$ and $\Delta G^{\ddagger}$ values of **(a)**–**(b)** O_3-initiated reactions and **(c)**–**(f)** $HO^{\bullet}$-initiated reactions at different reaction positions.

(a)

958
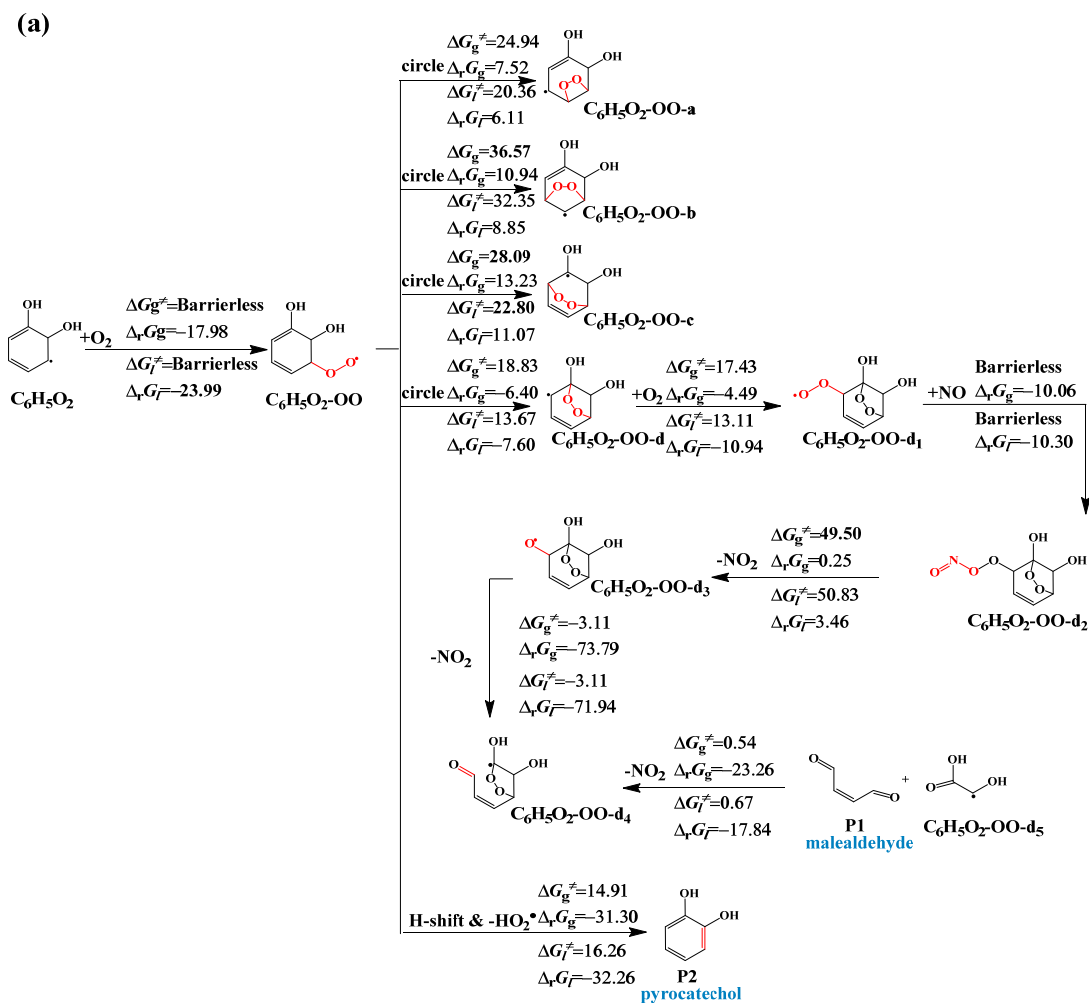
Fig.6 Subsequent reaction mechanisms of important intermediates (IMs) (unit: kcal mol $^{-1}$) in **(a)**

gas phase (g) / bulk water (l) and at **(b)** A-W interface (Continue on the next page).

961
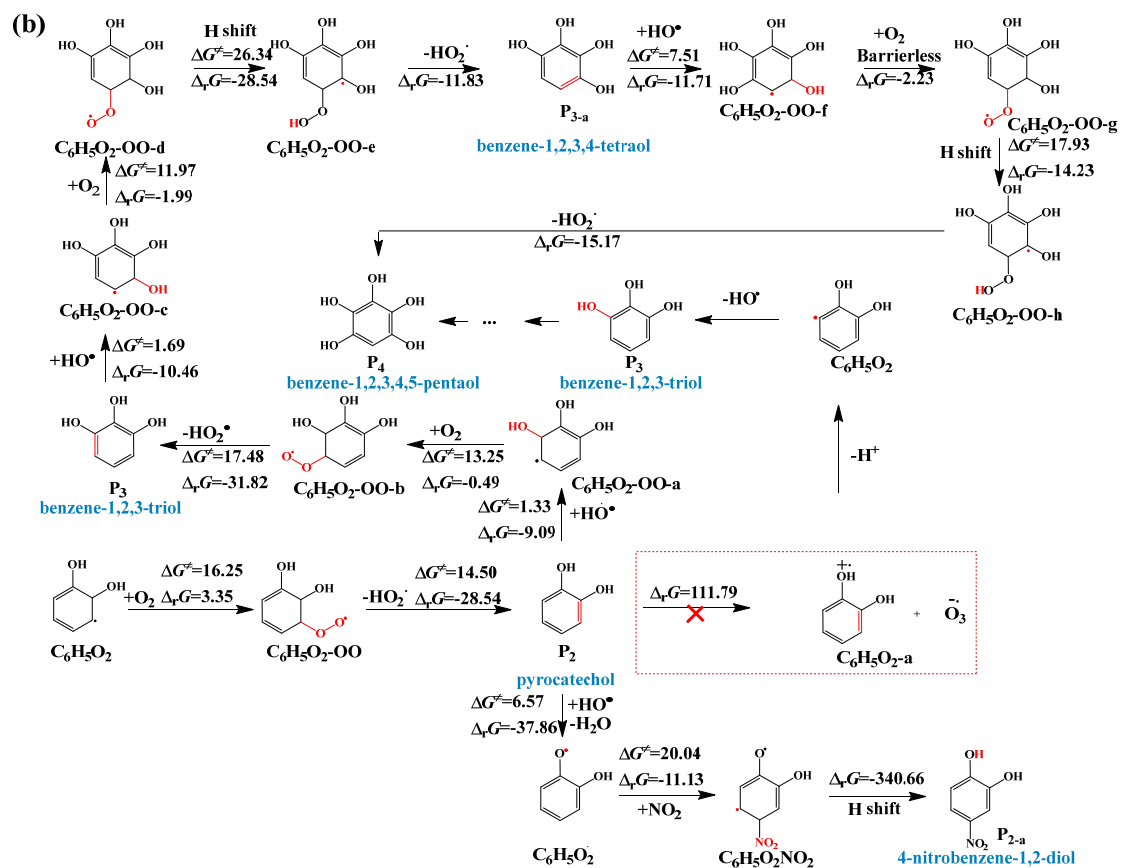
Fig.6 (Continue) Subsequent reaction mechanisms of important intermediates (IMs) (unit: kcal mol^{-1}) in **(a)** gas phase (g) / bulk water (l) and at **(b)** A-W interface.

969
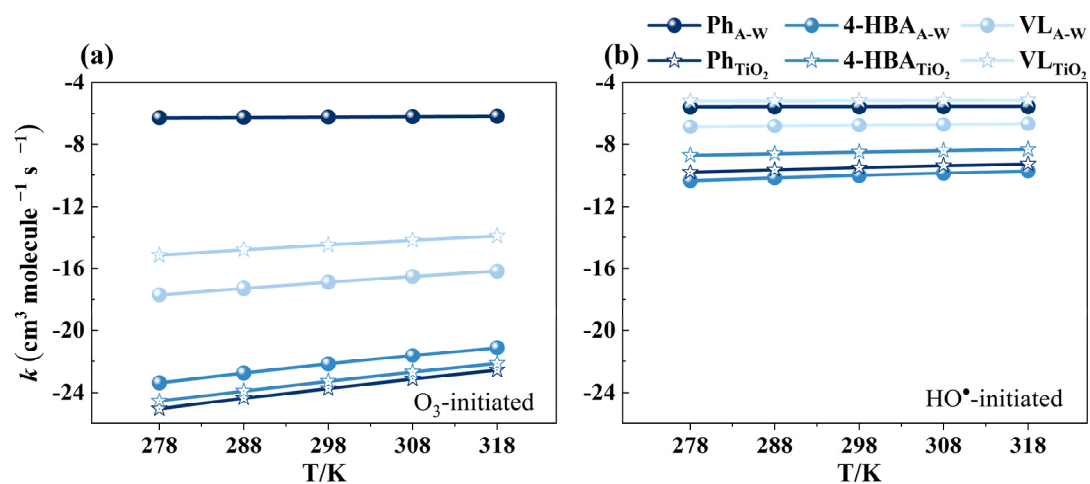
970   **Fig. 7** Calculated rate constants for the initial reactions of Ph, 4-HBA, and VL with O_3 and $HO^\bullet$ at

971   different temperatures (278–318 K) and 1 atm.

972

973

974

975

976

977

978

979

980

981

982

983

984

985

986   **Table 1** The available experimental and calculated reaction rate constants (k) values of O_3- and

987   HO•-initiated reactions at 298 K. Unit: cm^3 molecule $^{-1}$ s $^{-1}$.

Compounds	$k_{tot\text{-}A\text{-}W,cal}$[a]	$k_{tot\text{-}TiO_2,cal}$[b]	$k_{tot\text{-}gas,cal}$[c]	$k_{tot\text{-}wat,cal}$[d]	$k_{,exp}$	Ref.
Ph	5.98×10^{-7}	1.84×10^{-24}	5.27×10^{-20}	4.02×10^{12}	$(13.5 \pm 1.1) \times 10^{-18}$,[e]	Zein et al. (2015)
	2.69×10^{-6}	3.17×10^{-10}	2.34×10^{-9}	4.46×10^{13}	—	
4-HBA	6.79×10^{-23}	5.32×10^{-24}	4.93×10^{-24}	1.97×10^{12}	—	
	9.49×10^{-11}	3.16×10^{-9}	7.90×10^{-11}	2.52×10^{13}	—	Rana et al. (2020)
VL	1.27×10^{-17}	3.30×10^{-15}	1.35×10^{-22}	2.20×10^{12}	$(0.40 \pm 0.31) \times 10^{-18}$,[f]	Zein et al. (2015)
	1.73×10^{-7}	6.70×10^{-6}	1.14×10^{-10}	3.15×10^{13}	6.00×10^{-11},[g]	Rana et al. (2020)

988   [a]: calculated values of phenolic compounds at A-W interface;

989   [b]: calculated values of phenolic compounds on TiO_2 clusters;

990   [c]: calculated values of phenolic compounds in the gas phase;

991   [d]: calculated values of phenolic compounds in the bulk water.

992   [e]: experimental values of catechol in the gas phase;

993   [f]: experimental values of guaiacol in the gas phase;

994   [g]: experimental average $k_{HO•}$ values of methoxyphenols in the gas phase.